Evaluation of a novel noncontact spectrally and spatially resolved reflectance setup with continuously variable source-detector separation using silicone phantoms

Stefan Andree
Carina Reble
Technische Universität Berlin
Institut für Optik und Atomare Physik
10587 Berlin, Germany
and
Laser- und Medizin-Technologie, Berlin
Fabeckstraße 60-62
14195 Berlin, Germany

Jürgen Helfmann
Ingo Gersonde
Gerd Illing
Laser- und Medizin-Technologie, Berlin
Fabeckstraße 60-62
14195 Berlin, Germany

Abstract. We present a new variant of a noncontact, oblique incidence spatially resolved reflectance setup. The continuously variable source detector separation enables adaptation to high and low albedo samples. Absorption (μ_a) and reduced scattering coefficients (μ'_s) are determined in the wavelength range of 400–1000 nm using a lookup table, calculated by a Monte Carlo simulation of the light transport. The method is characterized by an silicone phantom study covering a wide parameter range 0.01 $mm^{-1} \leq \mu_a \leq 2.5\ mm^{-1}$ and 0.2 $mm^{-1} \leq \mu'_s \leq 10\ mm^{-1}$, which includes the optical parameters of tissue in the visible and near infrared. The influence of the incident angle and the detection aperture on the simulated remission was examined. Using perpendicular incidence and 90-deg detection aperture in the Monte Carlo simulation in contrast to the experimental situation with 30-deg incidence and 4.6-deg detection aperture is shown to be valid for the parameter range $\mu'_s > 1\ mm^{-1}$ and $\mu_a < 1.2\ mm^{-1}$. A Mie calculation is presented, showing that a decreasing reduced scattering coefficient for increasing absorption can be the consequence of real physics instead of cross talk.
 [DOI: 10.1117/1.3526367]

Keywords: backscattering; diffuse reflectance; turbid media; phantom studies; tissue optics; tissue optical parameters.

Paper 09544PRRR received Dec. 9, 2009; revised manuscript received May 31, 2010; accepted for publication Nov. 1, 2010; published online Dec. 23, 2010.

1 Introduction

For *in vivo* optical diagnostics and therapy in medicine, it is crucial to know the absorption and (reduced) scattering coefficients of the tissue under examination. Using integrating sphere spectrometer (ISS) measurements, which are considered the gold standard, requires the preparation of thin layers, which is time consuming and impossible for *in vivo* applications. Spatially resolved reflectance spectroscopy (SRR) is an optical method that is widely used to deduce these coefficients in geometries where transmission measurements are not possible. The applications range from treatment planning or dosimetry of laser therapy[1] to noninvasive tumor diagnostics[2,3] or simply determining the concentration of different absorbers, such as carotenoids, (de)oxyhemoglobin or bilirubin in tissue.[4–6] The optical properties determined from SRR can also be used to correct Raman signals by the influence of absorption and scattering.[7]

Instead of measuring only the total diffuse reflectance, which does not yield enough information, the remission of the tissue is detected at various distances from the illumination spot. The correlation between the remission and μ_a or μ'_s varies with distance.[8] This makes it possible to determine these parameters using an appropriate model for the light transport. The SRR method does not need specific assumptions for the spectral dependency of the absorption or reduced scattering coefficients, contrary to the single-fiber,[9] single-distance reflectance or differential path-length methods.[10] Most of the SRR variants use fiber applicators in contact with the sample and fixed distances between the fibers[3,4,11–15] or the detector is placed directly onto the sample surface.[16] In most cases, the results are obtained only for a single or a few wavelengths. Using fixed distances between fibers, one has the advantage of compact and simple-to-handle probe heads, but prior knowledge of the optical properties range is required in order to select the optimal fiber separations and diameters. It is also possible to use several lasers with a different wavelength or a broadband light source for illumination together with an imaging spectrometer to record reflectance spectras for several distances and retrieve μ_a, $\mu^{(\prime)}_s$, and/or g in a wavelength range all at once.[17,18] In this case, only one integration time can be used for all detection fibers and thus, the signal intensity of the detection fibers closer to the source must be attenuated to avoid saturation of the detector and still being able to receive strong enough signals from larger distances.

Further setups capture an image of the sample's surface remission with a CCD array.[19,20] Using a CCD array, the wavelength of the illuminating light must be varied sequentially with time in order to perform a spectroscopic measurement.

In contrast to other measurement configurations, which merely focus on very specific applications in skin diagnostics, our detection method is kept maximally flexible, enabling us to find optimal configurations for application specific, simplified fiber applicators and doing fundamental studies on critical

Address all correspondence to: Stefan Andree, Laser- und Medizin-Technologie, Berlin (LMTB), Fabeckstraße 60-62, 14195 Berlin, Germany. Tel: 49-308-449-2372; Fax: 49-308-449-2399; E-mail: s.andree@lmtb.de.

1083-3668/2010/15(6)/067009/12/$25.00 © 2010 SPIE

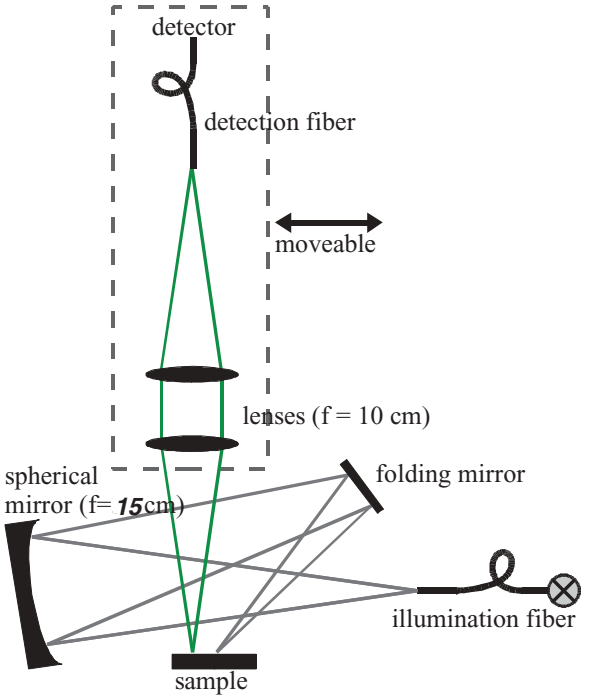

Fig. 1 Spatially resolved reflectance setup.

apparatus specific adjustments or critical steps in the retrieving procedure for the optical parameters.

By using the setup shown in Fig. 1, it is possible to acquire the remission in just one step over a wide spectral range.[21] For maximal versatility, the distance between the illumination and the detection area can be varied continuously and fibers with different diameters can be used. These can be interchanged for both source and detection, which enables the adjustment of the ratio between dynamic range and resolution. The difference between a spectral imaging system and ours is that we can adjust the integration time for every source-detector separation and do not need to attenuate the fiber signals dependent on the remission. Therefore, we can use a higher proportion of the incident light.

Because our setup is bigger than simple fiber applicators, it is not well suited for *in vivo* examinations but can be used for *in vitro* measurements of optical parameters for a wide range of absorption and reduced scattering coefficients. In order to evaluate the performance of our SRR variant, we carried out an extensive phantom study with silicone phantoms and compared the results to optical parameters determined from ISS measurements. A Monte Carlo (MC) simulation (MCS) was used to model the light transport because it does not rely on specific approximations, as the diffusion theory does, and is not limited to a certain range of absorption and reduced scattering coefficients.

2 Materials and Methods

2.1 *Experimental Setup for the Spatially Resolved Reflectance Method*

The experimental setup is presented in Fig. 1. A multimode fiber (numerical aperture, NA = 0.22) delivers light from a 7-W tungsten-halogen light source (⊗) by means of a spherical mirror (f = 15 cm, NA = 0.13) and a flat folding mirror onto the sample. The sample's surface is positioned in the image plane of the illumination optics. The magnification equals 1. Therefore, the spot size for illumination equals the fiber diameter, which is 400 μm. An oblique incidence of 30-deg is used to avoid the Fresnel reflection entering the detection beam path. The detection optics are made up of two achromatic lenses (f = 10 cm, NA = 0.08), which image the remission from an area of the sample surface with a magnification of 1 onto the detection fiber's end face. Once again, the spot size for the collection is 400 μm. The detection fiber and the corresponding optics can be moved continuously as a whole to change the source-detector separation. It is defined as the distance between the center of the illumination and detection spot. This enables radial scans of backscattered light to be obtained. An important aspect is the ability to measure the remission for negative and positive distances so that it is possible to check if the point of maximum overlap is at the distance zero.

The spectrometer used for detection has a spectral range from 200 to 1100 nm due to an integrated order filter, a wavelength resolution of 4 nm, 14 bit dynamic range, 300:1 full signal signal-to-noise ratio (SNR), and the entrance NA is matched to the detection fiber NA (HR4000 from Ocean Optics with 100-μm slit and HC1 grating). Considering also the fiber transmissions and the lamp spectral intensity, the measuring range was 400–1000 nm.

2.2 *Spatially Resolved Reflectance Measurements*

The measurements on the samples are carried out using a self-written LabVIEW program controlling the shutter of the halogen lamp, the spectrometer, and the piezomotor stages. The measurement is carried out automatically, except for the alignment of detection and illumination optics, which is done manually beforehand. The program records two spectra for every source-detector separation, one with illumination on and a dark spectrum with illumination off. The integration time is autoadjusted to receive a "light-on" signal between 90 and 100% of the saturation level. The integration time for the dark spectrum is set to the same value. The dark spectrum is subtracted from the first one, and the difference is saved to a file. The detection optics are moved according to tabulated distances (–0.5 mm, –0.4, –0.3, 0.20, –0.1, –0.05, 0, 0.05, 0.1, 0.2, 0.3, 0.4, 0.5, 0.6, 0.8, 1, 1.2, 1.4, 1.6, 1.8, 2 mm) between the illumination spot and the recording points of the remission profile. Data points from 0.5 mm distance and above are used for the determination of the optical properties. The negative distances are included because a means is required for checking if the origin of the distance axis is really at zero. To have a higher resolution for detecting a shift of the origin, we acquired the remission with a smaller step width near the origin. The autoadjustment of the integration time to the intensity of the remission is repeated after each movement. The different integration times are accounted for by dividing the signal by them. To estimate the statistical errors, the sample is moved laterally 0.1 mm after each scan and then a completely new remission profile is recorded. This is repeated five times, and then all remission profiles are averaged. The time needed for measuring the remission for one source-detector separation strongly depends on the sample absorption and scattering coefficient. It ranges from a second for high albedo, to tens of

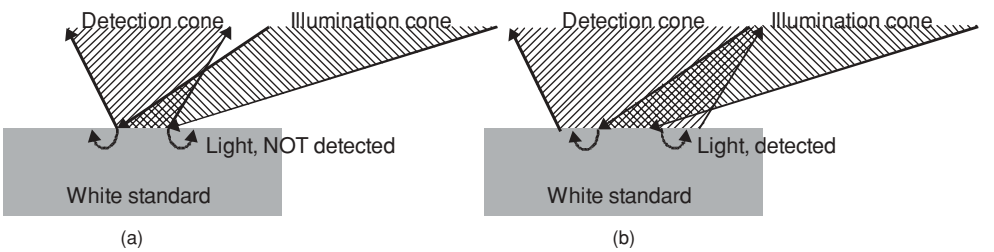

Fig. 2 (a) Equal illumination and detection area: Light remitted off the illumination spot is not detected. (b) Larger detection area than illumination area: Light remitted off the illumination spot is detected.

seconds for low albedo. Statistical errors are due to the detector noise, which contributes mainly for source-detector separations of >1.5 mm. The SNR varied between 50 for source-detector separations of <1 mm and 10 for the samples with the largest amount of absorber and source-detector separations of 2 mm. The halogen lamp was tested for time variations, and this effect could be excluded as a source of error. The motor for positioning of the detection optics is made for microscope applications and is far more exact than is needed for this SRR setup. Therefore, an uncertainty in source-detector separation can also be neglected. In contrast, the stray-light contribution to systematical errors must be considered because its signal overlaps with the remission signal. This effect becomes larger for larger source-detector separations. Therefore, it is necessary to protect all optical components against dust after establishing their cleanliness (not shown in Fig. 1).

2.3 *Normalization of the Spatially Resolved Measurement Data*

The measured reflectance spectra have to be normalized in order to correct them for the illumination efficiency of the light source, the collection efficiency of the fibers, and the spectrometer sensitivity, as well as being able to compare the measurement to the MCS. The aim of the normalization is to infer the power and spectral distribution of the illumination immediately before the light enters the sample. This is usually done by measuring the reflectance of a reference standard. Ideally, a nonabsorbing Lambertian surface reflector is needed for this but such a material is not available.

A pressed titanium dioxide (TiO_2) powder was used as a reference standard, and during preparation, a facial tissue was placed between the die and the powder to produce a rough surface. It is therefore assumed that the white standard is a Lambertian reflector. For a detection angle of 0 deg, and angles of incidence between 0 and 40 deg, this is validated by the measurements presented in Ref. 22 (see Chapter II-e). Titanium dioxide was measured in the ISS against Spectralon. Spectralon is a trade name for sintered polytetrafluorethylen and is a common white standard with a reflectance higher than 98% in the wavelength range of 400–1000 nm.[23] The measurement showed that titanium dioxide has a reflectance of >97% in the wavelength range between 450 and 1000 nm, with a maximum of 99% at 550 nm. From 450 to 400 nm, the reflectance decreases from 97 to 75%. In this range, the correction for the decrease in reflectance of titanium dioxide improves the determined optical properties of the phantoms by the SRR method. The calibration with the titanium dioxide standard was carried out in two steps: spectral calibration and intensity calibration. The spectral calibration is frequently carried out using the spectrometer and the same fibers that are used for the measurement of the sample. The intensity calibration is only carried out if the last measurement was taken several days prior. To perform the spectral calibration, both source and detection fibers have diameters of 400 μm. The illumination and detection fibers are positioned so that the illumination and detection spots overlap [Fig. 2(a)]. In this way, the spectral distribution of the reference is determined but some of the light is still remitted outside of the detection area and is not collected. This loss has to be quantified by the intensity calibration, which is done by comparing the total power delivered by a 550-μm-diam detection fiber with the delivered power of the 400-μm-diam fiber using a light power meter. The 550-μm-diam fiber detects all but a negligible part of the remitted light [Fig. 2(b)]. The ratio between the signal of the 400-μm detection fiber and the 550-μm detection fiber was 0.72. Using the titanium dioxide standard, a detection fiber with a 1000-μm diameter does not significantly increase the signal anymore, whereas using the Spectralon standard it does. The ratio between the signal of the 1000-μm detection fiber and the 550-μm detection fiber was then 0.82. A larger diameter fiber would be too stiff to be practical, which is the reason why we use titanium dioxide instead of Spectralon. The wavelength dependence of the signal from the titanium dioxide standard was measured with lasers and laser diodes of the wavelengths 425, 488, 532, 543, 633, 670, 750, and 820 nm. The ratio of the signals from the different detection fibers was 0.72 $\pm$ 0.05 for all laser wavelengths, and no systematic wavelength dependency was found.

Advantageously, we can determine the reference spectra from overlapping illumination and detection spot. If the reference spectrum is not measured with zero source-detector separation, then the relative contribution from different wavelengths to the signal will change, which is not desired. With fiber applicators, it is only possible to measure the remission of the white standard with a nonzero source-detector separation.

The data obtained from the phantom measurements is normalized according to Eq. (1), which is similar to the one presented in Ref. 24,

$$M(\lambda, r) = \frac{M_{\mathrm{Sample}}(\lambda, r)0.72}{M_{\mathrm{W}}(\lambda)} = \frac{L(\lambda)(1-F)S(\lambda, r)D(\lambda)}{L(\lambda)W(\lambda)D(\lambda)}. \quad (1)$$

The unnormalized reflectance values obtained by the measurement are M_{Sample} and M_{W} for the sample and the reference white standard, respectively. A wavelength dependency is denoted by λ, and radial dependency is denoted by r. The spectra

M_{Sample} and M_{W} are already divided by the corresponding integration time. For M_{Sample}, this is done separately for every source-detector separation. Both sample and reference spectra are measured with the same numerical aperture NA. The factor 0.72 in the reference measurement is due to the correction for the loss of photons when both 400-μm-diam fibers are used for source and detection as described above. The remissions for the sample and white standard are labeled S and W. L is the light-source power spectrum, D the detector efficiency, and F the Fresnel reflection coefficient. The light-source and detector characteristics cancel each other out, leaving S, W, and the factor $(1-F)$. This ratio can now be used to determine μ_a and μ'_s by comparison to the remission calculated by the MCS for a detection aperture of 90 deg. The factor $(1-F)$ is calculated from the refractive index n of the sample by the formula $(1–F) = 1-(n–1)/(n+1)$ and is $\sim$0.97 for the silicone phantoms discussed in Section 3 ($n=1.41$). The refractive index was determined from the Fresnel reflection of the silicone phantoms measured with the ISS. The MCS takes account of the Fresnel reflection, and therefore, the factor $(1–F)$ need not be considered explicit in the normalization. The surface reflection and volume backscattering of the white standard both contribute to the reference spectrum because pressed titanium dioxide has a rough surface and no specular reflection. Therefore, a factor $(1-F)$ is not needed for W.

2.4 *MCS*

To determine the absorption and reduced scattering coefficients from the measurement data, a numerical or theoretical model is needed to model the light transport through the sample. In our case, this is the MC simulation.

The light is regarded as a stream of particles, and so interference and polarization effects are neglected, which is valid for incoherent light sources such as halogen lamps. Although it is, strictly speaking, incorrect, here we will refer to these particles as photons. The basic principles of the MC algorithm are described in Ref. 25 (see Chapter 3). The MC algorithm launches photons at a specified position and with a specified direction distribution outside the medium and sends them onto a random walk through the medium. When the photons arrive at the sample surface, some are reflected according to Fresnel's formula and some are refracted according to Snell's law. Inside the medium, the particles can be absorbed, scattered, and/or total reflected at the surface or refracted again leaving the medium. Some of the escaped photons arrive at the detector within the acceptance angle and contribute to the signal. The main output of the MCS is the ratio between photons arriving at the detector and the total number of photons launched.

Determining the light distribution inside the sample from the absorption coefficient μ_a, reduced scattering coefficient μ'_s, scattering anisotropy g, refractive index n, and the experimental geometry is known as a forward problem. This is in contrast to the so-called inverse problem, where the coefficients μ_a, μ'_s, and g are determined from the measured detector signals.

2.5 *MCS of Spatially Resolved Reflectance*

The described forward MC algorithm (Section 2.4) was adapted to the SRR setup. With the SRR setup, the remission is measured for different source-detector separations. Therefore, the MCS should be able to calculate the remission for specified source-detector separations taking into account the size of illumination and detection spots, both numerical apertures of illumination and detection, the optical properties of the sample, and the sample size and thickness. When the optical properties of the sample do not change laterally and the illumination is normal to the surface, the probability of detecting a photon is dependent only on the distance between the entrance and exit point beside the dependence on the optical properties. This distance is different from the source-detector separation because the entrance and exit points can be anywhere inside the illumination and detection spots (Fig. 3). The simulation algorithm exploits this property, and therefore, oblique incidence is not supported. To gain the remission for a specific source-detector separation, the probability p for collecting a photon must be integrated over the illumination area A and the detection area A' to give the probability $p(r_{sd}) = \int_A dA \int_{A'} dA'\, p(|\boldsymbol{r}-\boldsymbol{r}'|)$. Here, r is a vector to a point in A, $\boldsymbol{r}'$ to a point in A' and r_{sd} is the source-detector separation. With a weighting function $w(r)$, this integral can be simplified to $p(r_{sd}) = \int_a^b dr\, w(r) p(r)$, where a is the smallest and b is the largest possible distance between entrance and exit points.[11]

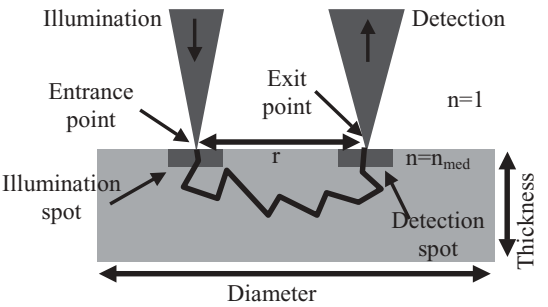

Fig. 3 Geometry for spatially resolved reflectance Monte Carlo. Illumination: Numerical aperture of illuminating light beam, Detection: Numerical aperture for collecting photons, n: refractive index, r: distance between illumination and detection spot.

The described MC algorithm was compared to multi layer Monte Carlo simulation (MCML),[12] which has already been accepted as the reference MCS in the tissue optics community. The data show excellent agreement between the two simulation algorithms for the perpendicular incidence case and μ_a ranging from 0.001 to 1.2 mm^{-1} as well as μ'_s ranging from 0.1 to 10 mm^{-1}.

The photons are launched with a constant probability distribution for the incidence direction within the illumination aperture. The focus is on the sample surface. The proportion of those photons that are not reflected by the surface are propagated through the sample until they exit the medium again. To calculate the probability $p(r)$ needed for the above integral, the number of detected photons leaving the sample at a certain distance r is divided by the number of incident photons. Only the photons with a direction within the numerical aperture of the detector contribute to the signal. The simulation does this numerical integration for all source-detector area separations used in the experiment.

The MCS replaces virtually the lower lens of the detection optics by a detector with the same diameter. It does not simulate

the light passing through the lenses and through the detection fiber. Nevertheless, as the acceptance angle of the collection fiber is larger than the aperture of the detection optics, and as the acceptance angle of the spectrometer equals that of the fiber, this should not lead to a discrepancy between simulation and measurement if the proper detection aperture is considered.

2.6 *Using a Lookup Table to Infer Absorption and Reduced Scattering Coefficient*

The forward MCS, which was adapted to SRR, was used to calculate a lookup table with remission profiles for many combinations of μ_a and μ'_s. A search algorithm was made to compare the table entries with the measurement data, consecutively. The absorption and reduced scattering coefficients corresponding to the best matching profile were then read from the table. In order to have a measure as to just how well a particular simulated remission profile matches with the measurement data, the program calculates the deviation $\eta(r)$ between the logarithms of simulated and measured data for each source-detector separation [Eq. (2)]. Then, the average is computed over all distances in a given range [Eq. (3)]. By this procedure, the noisier data points from larger source-detector separations are weighted less because the signal decreases with distance. By searching the profile with the smallest $\bar{\eta}$, μ_a and μ'_s of the sample can be determined. For all the simulations and measurements made in the phantom study described in Section 3, $\bar{\eta} < 0.06$,

$$\eta(r) = |\ln[M(r)] - \ln[M_{\mathrm{Sim}}(r)]|, \tag{2}$$

$$\bar{\eta} = \langle \eta(r) \rangle. \tag{3}$$

In our case, the source-detector separation was $0.5 \leq r \leq 2$ mm. The data points for lower distances were not included because the MCS cannot output remission values for distances lower than the fiber diameter due to the weighting procedure (see Section 2.5). The negative distances were omitted because they were only used to check the origin of the distance axis (see Section 2.2). The range was found to be stable against small variations of the beginning of the interval to the end of the interval (fitting over the range $0.4 \leq r \leq 1.8$ mm or $0.6 \leq r \leq 2.2$ mm gave the same results). Another reason for limiting the fitting range was that the measured signal gets too noisy for large distances ($r > 2$ mm, SNR < 10).

The lookup table calculated with the forward MCS, for the SRR samples had a size of 40×40 remission profiles. The number of simulated photons was 5×10^6. The 40 μ'_s values were varied within the range from 0.01 to 8 mm^{-1} and the 40 μ_a values ranged from 0.001 to 2.3 mm^{-1}. The table was calculated for a constant g of 0.8 and extended by linear interpolation along the grid lines. This results in a higher resolution for the determination of the optical parameters ($\Delta\mu_a = 0.007$ mm^{-1}, $\Delta\mu'_s = 0.02$ mm^{-1}). According to the experimental setup, the illumination beam convergence angle was set to 7.12 deg and the circular spot size on the sample surface to 400 μm. The detector is specified by the acceptance angle, which was set to 90 deg to save calculation time, although this is in contrast to the experiment (4.6-deg acceptance angle). The circular detection area was set to a diameter of 400 μm, which is again in agreement with the setup. To avoid having to create a new lookup table for every sample thickness, phantoms were made as thick as 1.5 cm so that they could be considered approximately semi-infinite for the investigated parameter range. Two MCS were conducted with μ_a set to zero and μ'_s set to 0.06 mm^{-1}, the lowest reduced scattering coefficient of the phantom set. In the first run, the thickness and radius of the sample were set to 1.5 and 1.75 cm, the real dimensions of the phantom. In the second run, the thickness and radius were set to 10 and 5 cm. The relative deviation between both simulations was <1% for all source-detector separations between 0 and 2 mm. All other phantoms have a higher reduced scattering coefficient and/or a higher absorption coefficient; thus, the assumption of semi-infinite samples should be true for all phantoms.

2.7 *Integrating Sphere Setup*

A double-beam ISS measurement with a subsequent inverse MCS (iMCS) served as an independent method for the determination of μ_a, μ'_s beside SRR. The essential part of the spectrometer (Lambda 900 from PerkinElmer) is the integrating sphere, as seen in Fig. 4. The sphere has two ports with sample holders along the direction of the incoming light. The sample is placed at the left port to collect the transmitted light. For the hemispherical transmission, the right port was closed with a Spectralon standard and for the diffuse transmission it was not. The sample is placed at the right port for acquisition of the hemispherical reflection of the sample. In order to avoid uncertainties in the assignment of Fresnel reflection and diffuse reflection, the reflection measurements were performed with a closed Fresnel port. The holder at the reflection port is tilted at an angle of 8 deg to the direction of the incident light. The detector is at the bottom of the sphere and shielded against direct reflexes of the walls by a baffle (not shown). The port diameters are 2 cm, and the spot size of the beam on the sample was 5 mm. The measurements were carried out in the spectral range from 400 to 1000 nm in agreement with SRR.

The accuracy of the spectra measured in the ISS is limited by the dark and reference spectra with an uncertainty of 0.5% (400–850 nm) and 2% (850–1000 nm), which is already the sum of both errors. The discrepancy in the accuracy is due to a detector change at 850 nm.

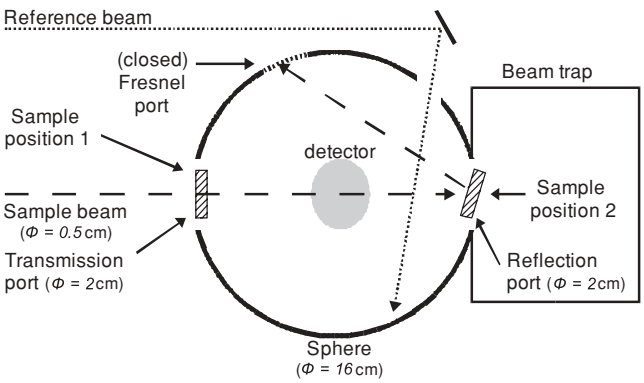

Fig. 4 Overview of the sample chamber of the integrating sphere spectrometer used as an independent method to evaluate SRR.

2.8 *Alternative Determination of μ_a and μ'_s Using an ISS*

An iMCS is used to relate either two spectra to μ_a and μ'_s or three spectra to μ_a, μ'_s, and g.[26] The iMCS algorithm was developed by the Laser-und Medizin-Technologie GmbH, Berlin especially for the PerkinElmer ISS described. The algorithm incorporates information about the sphere diameter, port sizes, beam width, and convergence, and the tilted sample holder as well, and takes account of it. The iMCS assumes a perfect glossy sample and an ideal reflecting sphere. This causes differences between the measured spectra and the simulated spectra for rough samples. In our case, the samples had a smooth surface so that the theoretical reflection coefficient agreed well with the real one.

The transmission and reflection are nonlinear functions of μ_a, μ_s, and the scattering phase function, which in our case was the one from Henyey-Greenstein.[28] If the selected values for the optical parameters correspond to the parameters of the sample, then the functions equal the measured transmission and reflection. Finding a solution for the optical parameters, for which the simulated and measurement spectra agree, is therefore equal to solving the system of the nonlinear equations for the transmission and reflection. For this task, the iMCS applies the Newton–Raphson root-finding algorithm.[27] The estimated spectra are calculated by a forward MCS. The optical parameters μ_a, μ'_s and the anisotropy of the phase function are varied according to the Newton–Raphson algorithm, until the computation result coincides within the error range to the measured spectra. The basis for the ISS forward MCS is the same as for the spatially resolved MC code (Section 2.5), which was compared to MCML.[12]

In our case, the sample index of refraction was set to $n = 1.41$ (silicone rubber) and the initial values were set to $\mu_a = 0.001\ \text{mm}^{-1}$ and $\mu'_s = 0.001\ \text{mm}^{-1}$ for every wavelength. For some samples, the influence of the start parameters on the determined optical properties were tested and there were only negligible differences found. The threshold error level for the termination of the iteration was set to 2%, which is also roughly the accuracy for the transmission and reflection. In case of the samples with 0 or 0.1% titanium dioxide, a difference was measured between the hemispherical and the diffuse transmission. Then, three spectra were given as input to the iMCS to determine μ_a, μ'_s, and g. As shown in Section 3.2, the average value for g was 0.8. This value was used for the other samples where hemispherical and diffuse transmission could not be distinguished. For the sake of comparison with SRR, we calculated μ'_s from μ_s and g. The samples were 1 mm thick and 1.5 cm in diameter, so that while using a spot size of 5 mm, we could neglect side losses out of the sample.

3 Phantom Studies

The aim of the phantom study was to compare μ_a and μ'_s gained from our SRR setup with μ_a and μ'_s determined by the independent ISS method. We made a set of silicone rubber phantoms (Wacker Elastosil RT 601 A + B). Both components (A and B) of the silicone are viscous, nontoxic fluids. Component B is a hardener that initiates an endothermic solidification process if mixed with component A in the ratio 1:9. The solidification takes place at room temperature within 24 h. The samples were places for 1 h into a desiccator to remove the air bubbles introduced during mixing. Any remaining air bubbles rise and burst within the curing time. The phantoms made in this way have a smooth surface that supports separation of specular and diffuse reflection. The specular reflection was determined from two ISS measurements with open and closed Fresnel ports and corresponded well with the Fresnel reflection calculated from the Fresnel formula. Titanium dioxide particles (P25, Degussa Hüls) with a broad size distribution from nanometer to micrometer were added as a scatterer, and a silicone color paste was added as an absorber (GE Bayer Silicones, Silopren LSR Color Paste Wine Red). The phantoms were stable for at least a period of one year. It is difficult to find dyes that dissolve and disperse homogenously in the silicone. However, this color paste is made especially for use with the silicone and does not exhibit these problems, but it is not a molecular dye and the data sheet states a particle size of 40 μm.

The phantom set consisted of ten basic phantoms with either no absorber or no titanium dioxide. They were used to check for the linear dependence of absorption and scattering coefficients on the concentration. Phantoms without absorber were made with 0.1, 0.3, 0.5, 0.7, and 0.9% titanium dioxide. Phantoms without titanium dioxide were made with 0.1, 0.2, 0.4, 0.57, and 0.8% color paste. The other 20 phantoms had all the combinations of absorber concentrations from 0.1, 0.2, 0.4, and 0.8% (mass fraction), as well as 0.1, 0.3, 0.5, 0.7, and 0.9% titanium dioxide. Two samples were made for each concentration, one with a thickness of ~1.5 cm, the second with a thickness of 1 mm. Both thick and thin samples were made from the same mixture to ensure that they had the same μ_a and μ'_s. The thicker phantoms were used for the SRR and the thinner ones for ISS measurements.

3.1 *Optical Properties of Silicone Rubber*

Silicone rubber is an optically clear and transparent material throughout the visible wavelength range. Transmission and reflection spectra (including Fresnel and diffuse reflection) of a solid silicone cylinder, 22 mm in height and 38 mm in diameter, were recorded with an integrating sphere spectrometer as described above. An IMCS with start values of $\mu_a = 0.001\ \text{mm}^{-1}$, $\mu'_s = 0.001\ \text{mm}^{-1}$, $g = 0$, and a sample index of refraction $n = 1.41$ was used to determine the optical parameters μ_a and μ'_s (Fig. 5).

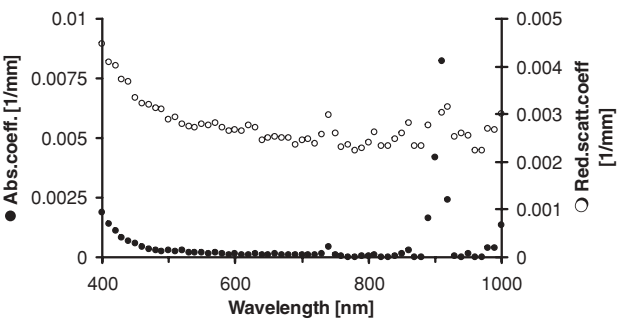

Fig. 5 Absorption (●) μ_a and reduced scattering coefficient (○) μ'_s of the silicone base material determined from the transmission and reflection spectra.

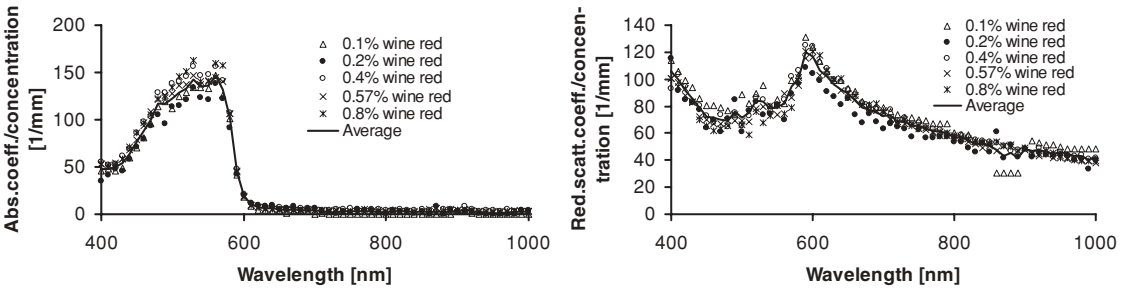

Fig. 6 Absorption μ_a and reduced scattering coefficient μ'_s divided by the concentration c (1% = 0.01) of the color paste containing phantoms determined by the ISS method for different absorber concentrations (relative difference: <15%).

The material has a low absorption ($\mu_a < 0.001$ mm^{-1}) and low scattering coefficient ($\mu'_s < 0.004$ mm^{-1}) between 400 and 1000 nm, except for 900 nm, where the silicone probably has a small absorption peak. Below 500 nm, there is a broad absorption band as well as increased turbidity in this wavelength range. With a magnifying glass, it was possible to see small amounts of impurities, such as dust particles, in the sample, which could lead to the higher scattering at shorter wavelengths. However, the absorption and scattering of the silicone rubber can be neglected compared to the absorption and scattering of the color paste and titanium dioxide in the 400–1000-nm wavelength range and the concentrations used.

3.2 *Optical Properties of the Basis Phantoms without Either Color Paste or Titanium Dioxide*

The color paste is a viscous, reddish looking, opaque fluid. We used the phantoms without titanium dioxide to determine the absorption and reduced scattering coefficients of the color paste dependent on its concentration (Fig. 6).

The measurements on the thin 1-mm phantoms were carried out with the ISS (see Section 2.8). As has already been shown in Section 3.1, the absorption and scattering of the base material can be neglected in the wavelength range between 400 and 1000 nm. Therefore, the data presented here are representative for the optical properties of the pure color paste. The material shows an absorption band below 600 nm, with the maximum absorption being located at 540 nm. The extrapolated absorption coefficient for 100% color paste is 150 mm^{-1} in the maximum. The μ_a range covered by the color paste concentrations 0.1–0.8% is 0.15–1.2 mm^{-1}. The reduced scattering coefficient is of the same order as the absorption coefficient. It is evident from this that the scattering coefficient of the color paste must be taken into account for all subsequent phantom measurements. Furthermore, μ'_s is considerably lower in the spectral range of high absorption and higher in the spectral range of low absorption. This effect looks like cross talk between the absorption and reduced scattering coefficient. Despite this, the anisotropy factor is approximately constant in the wavelength range of the absorption band (Fig. 7). The value of g varies between 0.73 and 0.81 with an average of 0.76. The ISS determined absorption and reduced scattering coefficient scale linearly with the concentration of the color paste.

From the samples without color paste, we only show the reduced scattering coefficient (Fig. 8) because the residual absorption coefficient was nearly constant over the wavelength range 400–1000 nm with an average of 0.01 mm^{-1} and independent of the concentration. The reduced scattering coefficient falls monotonically with wavelength. For the wavelength 1000 nm, it is about four times lower than for the wavelength 400 nm. Titanium dioxide at a concentration of 1% leads to a reduced scattering coefficient of 0.8 mm^{-1} at 400 nm and 0.18 mm^{-1} at 1000 nm. The anisotropy factor varies between 0.71 at 400 nm to 0.83 at 1000 nm with an average of 0.8 (Fig. 9).

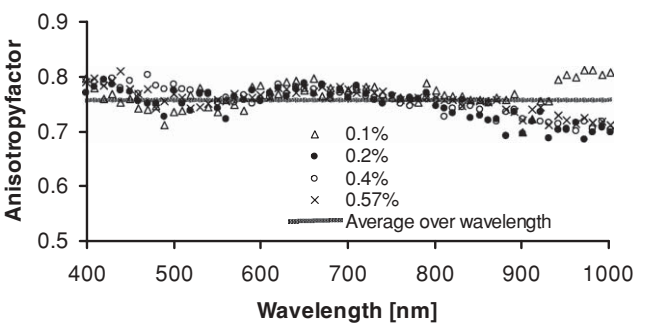

Fig. 7 Anisotropy factor g of the color paste determined by the ISS method for different absorber concentrations.

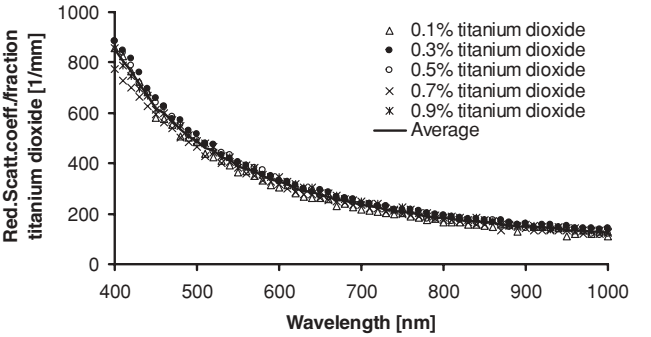

Fig. 8 Reduced scattering coefficient of titanium dioxide containing phantoms determined by the ISS method for different concentrations of titanium dioxide. The reduced scattering coefficient was divided by the concentration. (relative error <10%).

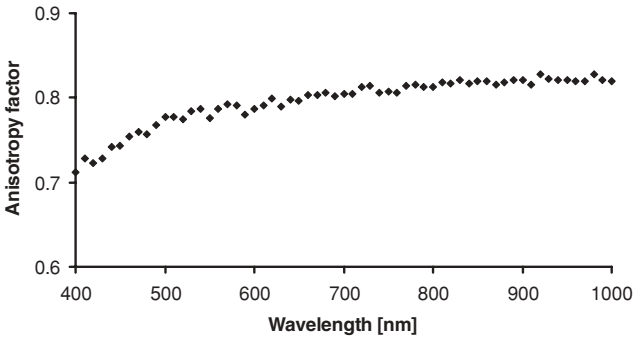

Fig. 9 Anisotropy factor of the phantoms without color paste determined by the ISS method.

3.3 *Optical Properties of the Phantoms with Color Paste and Titanium Dioxide*

After describing the basic materials, the results of the SRR and ISS measurements are described in this section for the entire set of phantoms. At first, we tested for the linearity of absorption and reduced scattering coefficients on the concentration of color paste and titanium dioxide, according to

$$\mu_a^{\text{expected}} = \mu_{a,\text{color paste}} \cdot c_{\text{color paste}} + 0.01\ \text{mm}^{-1}, \tag{4}$$

$$\mu_s'^{\text{expected}} = \mu'_{s,\text{TiO}_2} \cdot c_{\text{TiO}_2} + \mu'_{s,\text{ color paste}} \cdot c_{\text{color paste}}. \tag{5}$$

The label color paste stands for the spectra determined from the samples without titanium dioxide, whereas the label TiO_2 means, that the samples contained no color paste (Section 3.2) and c stands for the concentration. The titanium dioxide samples had a residual absorption of 0.01 mm^{-1}. This value was added to the term for the color paste. In contrast, the scattering properties of the color paste were considered with the second term of Eq. (5). The expected values were calculated from the ISS determined optical properties of the base phantoms.

The determined versus the expected values for the ISS measurements are shown in Fig. 10. The reduced scattering coefficient is linear to the concentration as shown by the straight solid line achieved from linear regression. The slope is 1.094 $\pm$ 0.004, which means that the determined values are, on average, 10% higher than the expected values over the range 0.2 $< \mu'_s <$ 10 mm^{-1}. The determined absorption coefficient is also linear to the concentration of the color paste and is about 14 $\pm$ 0.5% higher than expected in the range 0.04 $< \mu_a <$1.2 mm^{-1}, which was also achieved by linear regression. For expected absorption coefficients of $<$0.04 mm^{-1}, the data are too noisy and the true values cannot be resolved anymore.

Figure 11 shows the determined versus the expected absorption values from SRR measurements. The determined absorption coefficients of $>$0.04 mm^{-1} can be fitted by a straight line, which shows their linear dependence on the concentration. The values are 26 $\pm$ 1% larger than expected, which makes a difference of 12% between ISS and SRR absorption results. Absorption coefficients of $<$0.04 mm^{-1} could not be resolved anymore.

The same diagram for the reduced scattering coefficient is shown in Fig. 12. Most of the points accumulate along the ideal line, but some of the points have a large deviation from the expected values. This diagram does not resolve the dependence of the determined μ'_s on the expected μ_a. Therefore, these dependencies are shown in Fig. 12(b). The deviation is approximately constant for $\mu_a < 0.03$ mm^{-1}. For high μ_a and μ'_s, the deviation from expected is larger and negative compared to low μ_a and low μ'_s. There is cross talk between μ_a and μ'_s for expected μ_a larger than 0.03 mm^{-1}. In order to have a measure for the statistical errors, the systematic deviations can be fitted by polynomials in order to remove them (Fig. 13).

After the correction, there is still a considerable deviation left, but the improvement can be clearly seen. An evaluation

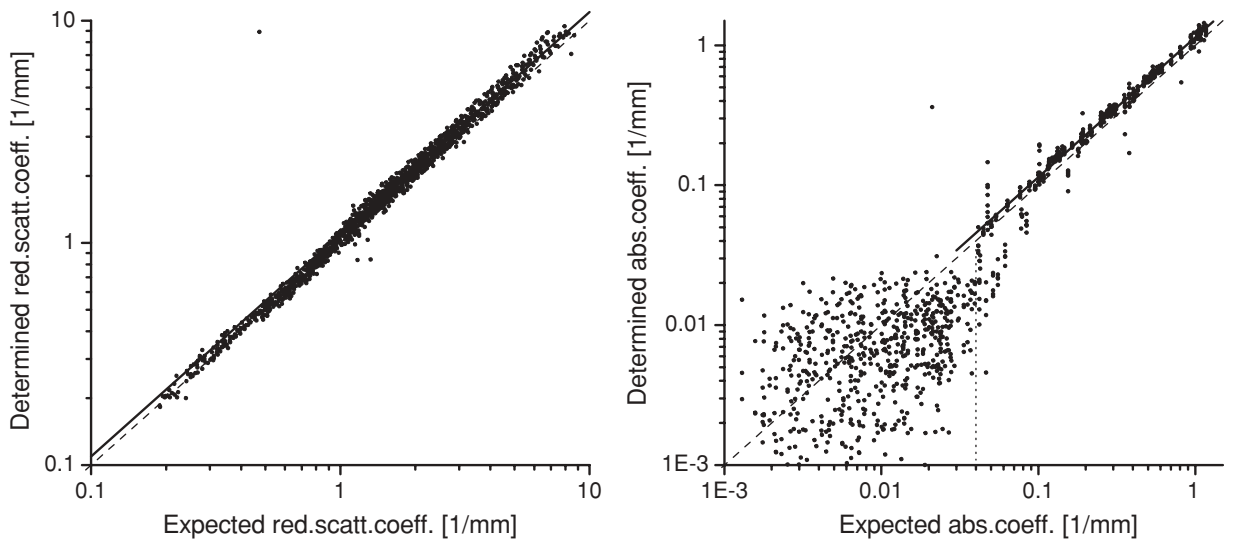

Fig. 10 Determined versus expected reduced scattering and absorption coefficients from ISS measurements. The data in the wavelength range 400–1000 nm of all but the basis phantoms were combined in these diagrams. The dashed lines indicate the ideal agreement. The solid lines are linear regression results ($\mu_s'^{\text{determined}} = 1.09\mu_s'^{\text{expected}}$, $\mu_a'^{\text{determined}} = 1.14\mu_a'^{\text{expected}}$). The vertical dotted line shows the lower limit of the measuring range.

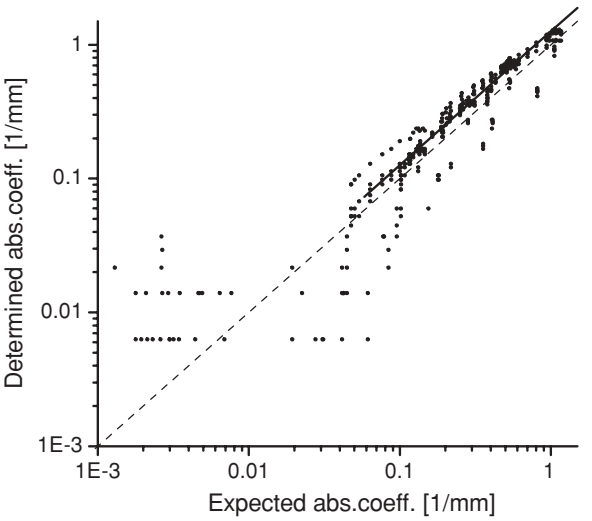

Fig. 11 Determined versus expected absorption coefficients from SRR measurements. The data in the wavelength range 400–1000 nm of all but the basis phantoms were combined in this diagram. The dashed lines indicate the ideal agreement. The solid line results from a linear regression ($\mu_a{}^{\text{determined}} = 1.26\mu_a{}^{\text{expected}}$).

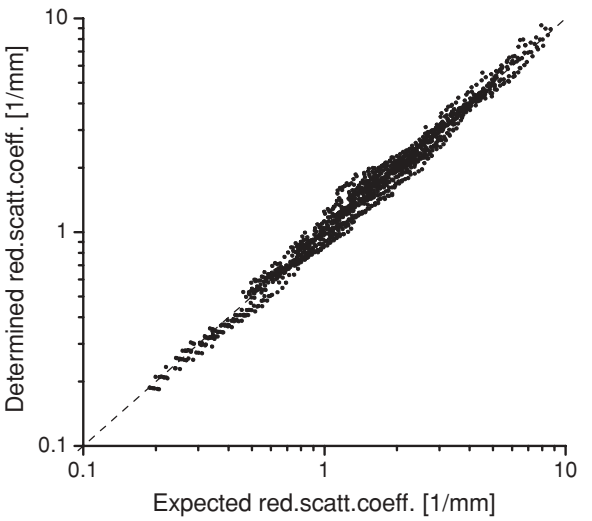

Fig. 13 Determined over expected reduced scattering coefficients from SRR measurements after correction for systematic deviations with a polynomial fit. The data in the wavelength range 400–1000 nm of all but the basic phantoms were combined in this diagram. The dashed line indicates ideal agreement.

showed that 70% of the data points have a deviation of <10% and 96% of <20%. This agrees with an average relative error of 10% of the absolute values.

3.4 *Comparison of Simulations for Perpendicular Incidence and 90-deg Detection Aperture to Simulations for 30-deg Incidence Angle and 4.6-deg Detection Aperture*

In order to investigate the influence of the incidence angle and detection aperture used in the simulation, we also conducted MCS for an oblique incidence angle of 30-deg and/or a detection solid angle of 4.6-deg, which corresponds to the geometry of the setup. With oblique incidence, the cylindrical symmetry cannot be exploited anymore resulting in worse photon statistics of the simulation result. A weighting function is also not used. The number of photons in each simulation was adjusted to similar SNR, such as in the simulation for perpendicular incidence and 90-deg detection aperture (10^8 instead of 5×10^6 photons).

Figure 14(a) shows a comparison of the MCS for both illumination and detection configurations for $\mu'_s = 0.5\ \text{mm}^{-1}$ and $\mu_a = 0.01$, 0.1, 0.6, or $1.2\ \text{mm}^{-1}$ (The error bars belong to the simulation with 30-deg incidence and 4.6-deg detection aperture). According to the Lambert cosine law, the remission for 90-deg detection aperture was multiplied by a factor $1 - \cos^2(4.6^\circ)$

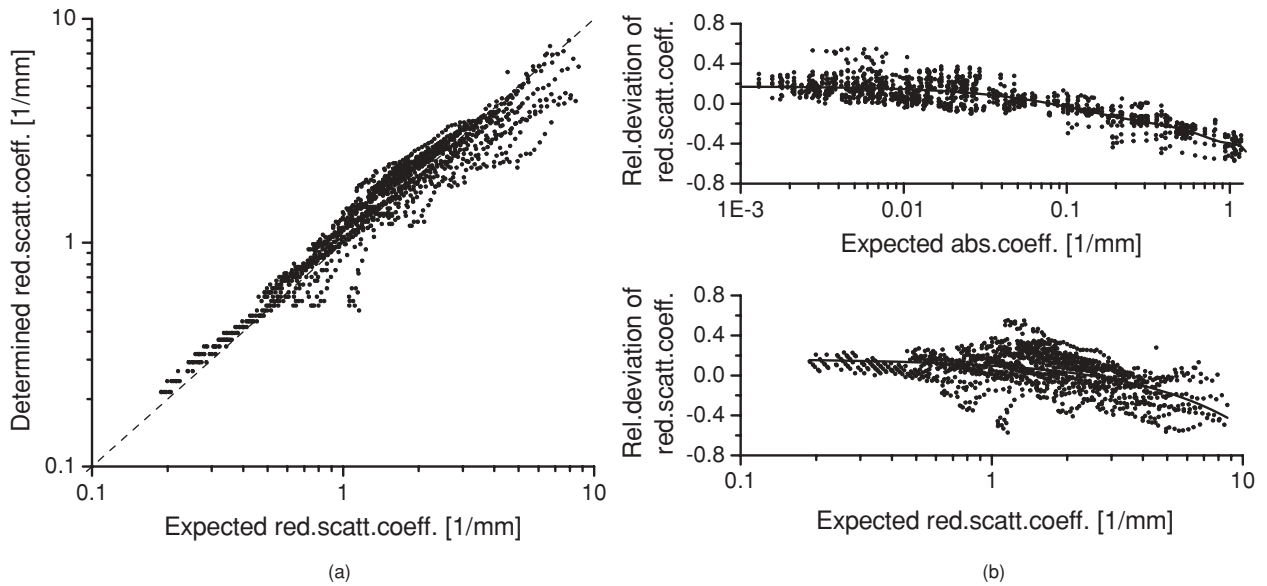

Fig. 12 (a) Determined over expected reduced scattering coefficients from SRR measurements. The data in the wavelength range 400–1000 nm of all but the basis phantoms were combined in this diagram. The dashed line indicates ideal agreement. (b) The relative deviation between determined and expected μ'_s values versus the expected μ_a and expected μ'_s. The solid line results from polynomial fits.

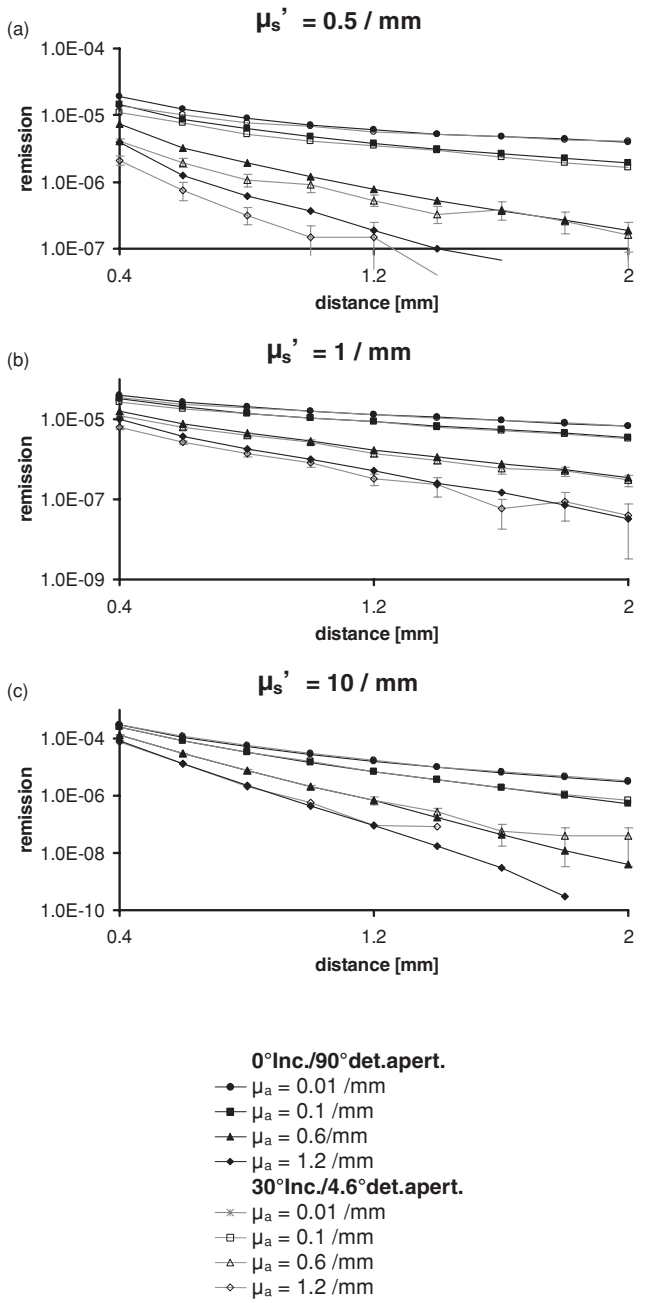

Fig. 14 Comparison of the MCS remission for both illumination and detection configurations (perpendicular incidence, 90-deg detection aperture versus 30-deg incidence /4.6-deg detection aperture) for μ'_s = 0.5, 2 and 10 mm^{-1}. The data for 90-deg detection aperture was multiplied by a factor 1-$\cos^2$(4.6 deg).

to make it comparable to the remission for 4.6-deg detection aperture. The remission for 30-deg incidence and 4.6-deg detection aperture is lower for short source detector separations, which is in agreement with the expectation that the remission becomes more and more Lambertian the higher the source detector separation is. The higher the absorption coefficient is the larger the range of distances is in which this discrepancy occurs. Figure 14(b) for $\mu'_s = 1\ mm^{-1}$ shows that the discrepancies for short source detector separations become lower than the uncertainty of the simulation results when μ'_s is increased. For $\mu'_s = 10\ mm^{-1}$ in Fig. 14(c) the deviation for short source detector separations disappears and there is only a deviation for $\mu_a = 0.6\ mm^{-1}$ for source detector separations of >1.2 mm. This is attributed to the bad SNR for these data points because the difference between both simulation results is lower than the uncertainty from the lack of simulated photons. For the simulation with $\mu_a = 1.2\ mm^{-1}$ and distances of >1.4, no photon was collected. Therefore, the data points are not shown.

This comparison of MCS with perpendicular incidence and 90-deg detection aperture versus 30-deg incidence and 4.6-deg detection aperture showed that the assumption of Lambertian remission of the samples is valid for $\mu'_s > 1\ mm^{-1}$ and $\mu_a < 1.2\ mm^{-1}$. This is true for the phantoms with 0.3–0.9% titanium dioxide and 0.1–0.8% color paste, which renders our normalization procedure valid for these samples. For the samples without titanium dioxide, the precondition is not fulfilled and, therefore, we could only use the integrating sphere measurements from these samples.

4 Discussion

The integrating sphere determined optical parameters presented in Sections 3.1–3.3 showed the linear dependence on color paste and titanium dioxide concentrations for $0.2 < \mu'_s < 10\ mm^{-1}$ and $0.04 < \mu_a < 1.2\ mm^{-1}$ (Fig. 10). For absorption coefficients of $<0.04\ mm^{-1}$, the statistical errors in the collimated transmission due to the detector noise became larger than the absorbed fraction of the incident light. However, if the samples were made thicker to increase the absorbed energy fraction, the difference between collimated and diffuse transmission would decrease, making it difficult to determine the anisotropy factor. On the other hand, it is necessary to determine the anisotropy factor from the samples with low color paste and titanium dioxide concentrations to use it as an input for the inverse MCS of the other samples with higher concentrations. Also, a means is required to test if the assumption of $g = 0.8$ is valid over the whole wavelength range for the SRR lookup table.

Considering the SRR-determined absorption coefficient (Fig. 11), the quantization of the lookup table can be seen for absorption coefficients of $<0.04\ mm^{-1}$. Therefore, this is a lower limit of the measuring range, though not a principal one. But also the relative deviation from the expected absorption coefficient becomes very large. Figure 12 shows that the determined μ'_s depends strongly on the absorption coefficient. Consequently, there must be still a systematic error in the SRR method, which we do not understand. The SRR method tends to overestimate μ_a about 10% and μ'_s for $\mu_a < 0.1\ mm^{-1}$ up to 20%, while it tends to underestimate μ'_s for $\mu_a > 0.1\ mm^{-1}$ up to 40%.

Swartling et al. compared spatially resolved and time-resolved diffuse reflectance measurements performed with an applicator consisting of a center illumination fiber and concentric detection fibers with a diffusion and a MCS model.[29] The fiber applicator consisted of fibers with 250-μm-diam and 0.6–7.8 mm source detector separations. Their experiment was performed with absorption coefficients in the range $0.001 < \mu_a < 0.05\ mm^{-1}$ and $0.5 < \mu'_s < 2\ mm^{-1}$. The absorber was toner from a copying machine. The fiber-based probe was calibrated with known standards. They found that there was a tendency to overestimate μ_a and underestimate μ'_s by the SRR in comparison to integrating sphere reference measurements. As written

above, we also found this behavior for absorption coefficients of $>0.1\ \mathrm{mm}^{-1}$. Like the color paste used in this study, they used an absorber with nonvanishing scattering. In the following, we examine and/or exclude different sources of error.

Because inhomogeneities have a higher impact on the ISS-determined optical parameters, we tested the homogeneity of the 1-mm-thick samples by varying the sample position relative to the illumination beam and comparing the iMCS results. There were only marginal differences. The variance of the thickness measurements of the 1-mm-thick phantoms was evaluated, and we determined the optical parameters for each of the smallest and largest thickness. The results show that the phantoms were prepared well and that weighing errors, errors due to insufficient mixing, or errors due to inaccurate thickness measurements can be disregarded.

We have shown that the samples for the SRR measurements could be considered as being semi-infinite and that they had a smooth surface. We also tested for differences between the optical parameters determined from the top and bottom of the samples to exclude errors due to settled titanium dioxide or a gradient in the color paste concentration. The measurements made on the top and bottom were consistent with one another. The thin phantoms measured in the ISS were made from the same mixture at the same time as the thick SRR samples and did not show significant deviations from the expected values.

Positioning of the detection optics is more exact than is needed, and an error due to inexact source-detector separation would lead to wrong parameters for the whole phantom set. Stray light in the setup would have had the contrary effect, because it would have increased the measured signal and would have led to a underestimation of the absorption coefficient. It was also possible to reproduce two measurements on one sample with maladjustment and new adjustment between the measurements. When considering the right incidence angle and detection aperture, there may be still an error introduced by the normalization procedure. It was found that the uncertainty in the measurement of the titanium dioxide and the determination of the factor 0.72 with 400 and 550 μm detection fibers (Section 2.3) is too low to explain the deviations found between SRR-determined μ_a and μ'_s and the expected values.

To explain the decrease in μ'_s in the absorption band range, which occurs for both ISS and SRR, we present a Mie calculation. Our Mie algorithm is based on the one of Bohren and Huffman.[30] The color paste is of particulate nature with a mean particle size of 40 μm (according to product data sheet). This explains that the color paste is also scattering. The color paste does not contain 100% pigment. This means that the absorption coefficient of a single particle (internal absorption coefficient) is probably significantly higher than that of the pure paste. However, this lower estimate of the absorption coefficient can be used as input for a Mie calculation with a sphere size of 40 μm (although the pigments in the color paste are probably of irregular shape), a sphere refractive index of 1.6, and a medium refractive index of 1.41 (Fig. 15). The medium index is that of silicone. The internal absorption coefficient of the sphere, indeed, has influence on the reduced scattering cross section, which shows that the decrease of the reduced scattering coefficient within the absorption band is probably a physical effect of the sample.

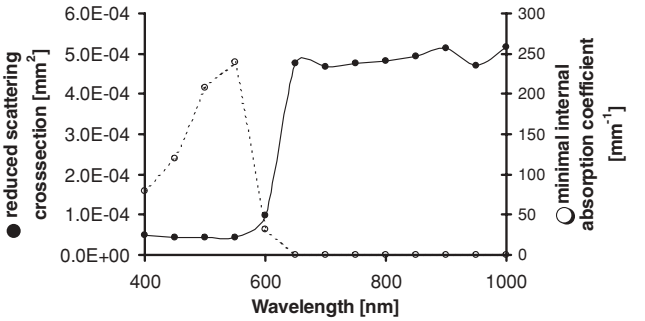

Fig. 15 Mie calculation of the scattering cross section for an absorbing sphere with a diameter of 40 μm, a refractive index of 1.6 in a medium with a refractive index of 1.4, and varying internal absorption coefficient.

Outside the absorption band, the reduced scattering cross section is approximately constant, which is not true for the phantoms. The phantoms contain the scattering substance titanium dioxide. The reduced scattering coefficient of the phantoms shows a power law dependence on the wavelength between 600 nm and 1000 nm. Titanium dioxide is not taken account for in the Mie calculation. This explains why μ'_s is constant for 600 nm–1000 nm in the Mie calculation in contrast to μ'_s of the phantoms.

5 Conclusion and Outlook

We evaluated a new, noncontact variant of a spectrally and spatially resolved reflectance system with continuously variable source-detector separation for wavelengths between 400 and 1000 nm using phantoms with color paste and titanium dioxide. The optical parameters were determined by means of a MC generated lookup table with perpendicular incidence and 90-deg detection aperture. By comparison to MCSs with 30-deg incidence and 4.6-deg detection aperture, which is in agreement with the illumination and detection configuration of the setup, it was shown that the lookup table is valid for samples with $\mu'_s > 1\ \mathrm{mm}^{-1}$ and $\mu_a < 1.2\ \mathrm{mm}^{-1}$. In this range, the remission of the sample can also assumed to be Lambertian, which is necessary for applying the normalization. Consequentially, a factor of 20 in the number of incident photons and thus calculation time can be saved.

The results determined by the lookup table were compared to the independent ISS method in the range $0.01 \le \mu_a \le 2.5\ \mathrm{mm}^{-1}$, $0.2 \le \mu'_s \le 10\ \mathrm{mm}^{-1}$, and the same wavelength region.

The result was, that SRR tends to overestimate μ_a about 10% and μ'_s for $\mu_a < 0.1\ \mathrm{mm}^{-1}$ up to 20%, while it tends to underestimate μ'_s for $\mu_a > 0.1\ \mathrm{mm}^{-1}$ up to 40%.

When the systematic deviations between SRR-determined optical parameters and expected ones are numerically removed, the statistical errors can be estimated to 10% of the absolute μ_a and μ'_s. Nevertheless, the introduced SRR setup looks promising as a means of determining optical parameters of turbid materials with a high spectral resolution. It has advantages over fiber-bundle applicators used in conjunction with imaging spectrometers, because the source-detector separation is continuously variable and there is no need to attenuate the signals for short source-detector separations.

We are also currently testing a potential solution to overcome the large calculation time for the lookup table with the right incidence angle and detection by setting up a lookup table made up of measured data only, as was done in Ref. 31.

Acknowledgments

The research project was funded by the Berlin Senate and co-financed by the European Union (European funds for regional development, FKZ 10138595). The authors would also like to thank the reviewers for their insightful comments on our manuscript.

References

1. A. Roggan, G. Müller (Ed.), and Berlien (Ed.), *Dosimetrie thermischer Laseranwendungen in der Medizin*, Dissentation, Fortschritte in der Lasermedizin **16**, Ecomed, Landsberg/Lech (1997).
2. D. Arifler, R. A. Schwarz, S. K. Chang, and R. Richards-Kortum, "Reflectance spectroscopy for diagnosis of epithelial pre-cancer; model-based analysis of fiber-optic probe designs to resolve spectral information from epithelium and stroma," *Appl. Opt.* **44**(20), 4291–4305 (2005).
3. C. Zhu, G. M. Palmer, T. M. Breslin, F. Xu, and N. Ramanujam, "Use of a multiseparation fiber optic probe for the optical diagnosis of breast cancer," *J. Biomed. Opt.* **10**(2), 024032 (2005).
4. E. Häggblad, T. Lindbergh, M. G. Karlsson, H. Casimir-Ahn, E. G. Salerud, and T. Strömberg, "Myocardial tissue oxygenation estimated with calibrated diffuse reflectance spectroscopy during coronary artery bypass grafting," *J. Biomed. Opt.* **13**(5), 054030 (2008).
5. H.-W. Wang, J.-K. Jiang, C.-H. Lin, J.-K. Lin, G.-J. Huang, and J.-S. Yu, "Diffuse reflectance spectroscopy detects increased haemoglobin concentration and decreased oxygenation during colon carcinogenesis from normal to malignant tumors," *Opt. Express* **17**(4), 2805–2817 (2009).
6. R. M. P. Doornbos, R. Land, M. C. Aalders, F. W. Cross, and H. J. C. M. Sterenborg, "The determination of *in vivo* human tissue optical properties and absolute chromophore concentrations using spatially resolved steady-state diffuse reflectance spectroscopy," *Phys. Med. Biol.* **44**(4), 967–981 (1999).
7. C. Reble, I. Gersonde, S. Andree, J. Helfmann, and G. Illing, "Quantitative Raman spectroscopy in turbid media," *J. Biomed. Opt.* **15**(3), 037016 (2010).
8. D. Arifler, "Sensitivity of spatially resolved reflectance signals to coincident variations in tissue optical properties," *Appl. Opt.* **49**(22), 4310–4320 (2010).
9. S. C. Kanick, H. J. C. M. Sterenborg, and A. Amelink, "Empirical model of the photon path length for a single fiber reflectance spectroscopy device," *Opt. Express* **17**(2), 860–871 (2009).
10. A. Amelink and H. J. C. M. Sterenborg, "Measurement of the local optical properties of turbid media by differential path-length spectroscopy," *Appl. Opt.* **43**(15), 3048–3054 (2004).
11. G. M. Palmer and N. Ramanujam, "Monte Carlo based inverse model for calculating tissue optical properties: Part I," *Appl. Opt.* **45**(5), 1072–1078 (2006).
12. L. H. Wang, S. L. Jacques, and L.-Q. Zheng, "MCML—Monte Carlo modeling of photon transport in multi-layered tissues," *Comput. Methods Programs Biomed.* **47**(2), 131–146 (1995).
13. T. P. Moffitt and S. A. Prahl, "Determining the reduced scattering of skin *in vivo* using sized—fiber reflectometry," *Proc. SPIE* **4613**, 254–263 (2002).
14. G. Zonios and A. Dimou, "Light scattering spectroscopy of human skin *in vivo*," *Opt. Express* **17**(3), 1256–1267 (2009).
15. G. Zonios and A. Dimou, "Modeling diffuse reflectance from semi-infinite turbid media: application to the study of skin optical properties," *Opt. Express* **14**(19), 8661–8674 (2006).
16. B. Yu, J. Y. Lo, and T. F. Kuech, et al., "Cost-effective diffuse reflectance spectroscopy device for quantifying tissue absorption and scattering *in vivo*," *J. Biomed. Opt.* **13**(6), 060505 (2008).
17. M. G. Nichols, E. L. Hull, and T. H. Foster, "Design and testing of a white-light, steady-state diffuse reflectance spectrometer for determination of optical properties of highly scattering systems," *Appl. Opt.* **36**(1), 93–104 (1997).
18. Q. Wang and H. Yang, A. Agrawal, "Measurement of internal tissue optical properties at ultraviolet and visible wavelengths: development and implementation of a fiberoptic-based system," *Opt. Express* **16**(12), 8685–8703 (2008).
19. A. Kienle and C. Wetzel, "Determination of the optical properties of anisotropic biological media using an isotropic diffusion model," *J. Biomed. Opt.* **12**(1), 014026 (2007).
20. M. Pilz, S. Honold, and A. Kienle, "Determination of the optical properties of turbid media by measurements of the spatially resolved reflectance considering the point-spread function of the camera system," *J. Biomed. Opt.* **13**(5), 054047 (2008).
21. S. Andree, C. Reble, J. Helfmann, I. Gersonde, and G. Illing, "Spatially resolved reflectance used to deduce absorption and reduced scattering coefficients," *Proc. SPIE* **7368**, 73680I (2009).
22. G. Kortüm, *Reflectance Spectroscopy*, Springer, New York (1969).
23. "A guide to reflectance coatings and materials," ⟨http://www.labsphere.com/data/userFiles/A%20Guide%20to%20Reflectance%20Coatings%20and%20Materials.pdf⟩ (20 April 2010).
24. S. Jacques, "Skin optics summary," ⟨http://omlc.ogi.edu/news/feb06/skinspect/slide4.htm⟩ (2006).
25. L.-H. Wang and H.-I. Wu, *Biomedical Optics—Principles and Imaging*, Wiley-Interscience, Hoboken, NJ (2007).
26. M. Friebel, A. Roggan, G. Müller, and M. Meinke, "Determination of optical properties of human blood in the spectral range 250 to 1100 nm using Monte Carlo simulations with hematocrit-dependent effective scattering phase functions," *J. Biomed. Opt.* **11**(3), 034021 (2006).
27. W. H. Press, B. P. Flannery, S. A. Teukolsky, and W. T. Vetterling, *Numerical Recipes in Pascal—The Art of Scientific Computing*, Cambridge University Press, Cambridge, England (1989).
28. L. G. Heneyey and J. L. Greenstein, "Diffuse radiation in the galaxy," *Astrophys. J.* **93**, 70–83 (1941).
29. J. Swartling, J. S. Dam, and S. Andersson-Engels, "Comparison of spatially and temporally resolved diffuse-reflectance measurement systems for determination of biomedical optical properties," *Appl. Opt.* **42**(22), 4612–4620 (2003).
30. C. F. Bohren, and D. R. Huffman, *Absorption and Scattering of Light by Small Particles*, Wiley, Hoboken, NJ (1983).
31. N. Rajaram, T. H. Nguyen, and J. W. Tunnell, "Lookup table-based inverse model for determining optical properties of turbid media," *J. Biomed. Opt.* **13**(5), 050501 (2008).